nature communications

Article

https://doi.org/10.1038/s41467-024-52006-0

Self-immolative poly(thiocarbamate) with localized H_2S signal amplification for precise cancer imaging and therapy

Received: 5 December 2023

Accepted: 22 August 2024

Published online: 30 August 2024

Check for updates

Qingyu Zong[1,5], Jun Li[2,5], Qing Xu[3], Ye Liu[1,2], Kewei Wang[3] & Youyong Yuan[2,3,4]

Hydrogen sulfide is essential in numerous physiological and pathological processes and has emerged as a promising cancer imaging and signaling molecule and a potentially versatile therapeutic agent. However, the endogenous levels of hydrogen sulfide remain insufficient to perform its biological functions, and thus, developing novel strategies that amplify hydrogen sulfide signals at lesion sites is of increasing interest. In this work, a nanoplatform (SNP) based on hydrogen sulfide-responsive self-immolative poly(-thiocarbamate) with localized hydrogen sulfide signal amplification capability is developed to encapsulate a hydrogen sulfide-responsive fluorescent probe (e.g., hemicyanine dye; p-Cy) or an anticancer prodrug (e.g., doxorubicin; p-DOX) to form a nanoprobe ($SNP_{p\text{-}Cy}$) or nanomedicine ($SNP_{p\text{-}DOX}$) for cancer imaging and therapy, respectively. $SNP_{p\text{-}Cy}$ exhibits a low detection limit for hydrogen sulfide, enabling ultrasensitive detection of small (<2 mm) tumors in female mice. In addition, $SNP_{p\text{-}DOX}$ can effectively inhibit the growth of DOX-resistant human breast cancer xenograft, lung metastasis, and patient-derived xenograft tumors in female mice.

Hydrogen sulfide (H_2S) is a crucial gas transmitter that controls numerous pathological and physiological actions[1–4]. Abnormal concentrations and tissue distributions of H_2S have been linked to diseases such as hepatitis, hypertension, diabetes, and cancer[5,6]. Recent studies have shown that endogenous or low levels of H_2S may result in pro-cancer effects, whereas an abundance of H_2S may cause cancer suppression[7,8]. Hence, H_2S has emerged as a promising cancer imaging and signaling molecule and a potentially versatile therapeutic agent[9–12], and the generation of a high concentration of H_2S is often aided by the gas delivery from H_2S donors in studies[13–16]. Various small molecule or polymeric H_2S donors can release H_2S when exposed to stimuli such as reactive oxygen species, pH, external light, and enzymatic activity[17,18]. Nevertheless, the generated H_2S may react with stimulus signals that decrease its level, causing inefficient H_2S delivery and insufficient H_2S to perform the intended biological functions. Thus, developing novel strategies that specifically amplify H_2S signals at lesion sites may be essential for advancing exogenous H_2S delivery.

Polymers that exhibit a response to exogenous (e.g., light irradiation or magnetic fields) or endogenous (e.g., acidic pH or reductive milieu) stimuli offer potential strategies for delivering theranostic agents to specific locations[19–25]. When exposed to specific stimuli, classical polymer disassembly occurs via a one-to-one degradation approach[26,27]. Conversely, self-immolative polymers can spontaneously degrade from head to tail via domino-like disassembly when the extremum is stimulated[28–31]. However, the complete degradation of conventional self-immolative polymers could only be accomplished when exposed to a stoichiometric quantity of triggering stimuli equal to that of stimulated by the capping agents. Inspired by the

[1]School of Medicine, South China University of Technology, Guangzhou 510006, China. [2]National Engineering Research Center for Tissue Restoration and Reconstruction, South China University of Technology, Guangzhou, China. [3]School of Biomedical Sciences and Engineering, South China University of Technology, Guangzhou International Campus, Guangzhou, China. [4]Guangdong Provincial Key Laboratory of Biomedical Engineering, South China University of Technology, Guangzhou, China. [5]These authors contributed equally: Qingyu Zong, Jun Li. e-mail: yuanyy@scut.edu.cn

amplification of communication signals between cells[32], studies have reported that amplified stimulus signaling can improve the sensitivity of biomarker detection, accelerate the degradation of the polymer to release drugs, and improve the activation efficiency of prodrugs[33–40]. Therefore, self-immolative polymers that can amplify stimulus signals have been proposed[41–43]. For such polymers, the degradation products of the trace activation chains could further drive the degradation of the remaining polymers, thereby allowing the specific stimulus to be amplified exponentially. Given the crucial role of H_2S plays in regulating physiological and pathological processes, the development of an innovative self-immolative polymer that amplifies H_2S signals in situ is essential yet challenging.

Here, we show a H_2S-responsive self-immolative poly(-thiocarbamate) (PTC) that amplifies the local H_2S signal for precise cancer imaging and therapy. We use benzyl thiocarbamates as the repeat unit of PTC in which released carbonyl sulfide (COS) through the specific stimuli triggered the 1,6-benzyl elimination reaction, for instance of H_2S (H_2S–PTC). Subsequently, the released COS is promptly hydrolyzed to H_2S by carbonic anhydrase (CA)[44], which further accelerates the degradation of the polymers in a positive feedback manner, resulting in an exponential polymer degradation cascade. More importantly, this polymer may act as an endogenous H_2S donor that releases multiple equivalents of H_2S per triggering event, enabling the endogenous H_2S signal to be rapidly amplified (Fig. 1 a, b). Notably, the tumor microenvironment is more H_2S-abundant than that of healthy tissues[45], which naturally endowed H_2S–PTC with tumor-specific H_2S release. Therefore, we conjugate carboxyl-terminated methoxy poly(ethylene glycol) (mPEG–COOH) on the terminal chain of H_2S–PTC to acquire the amphiphilic polymer (H_2S–PTC–PEG), which self-assembled into nanoparticles (SNP) and encapsulates a H_2S-responsive fluorescent probe based on hemicyanine dye (p-Cy) or anticancer prodrug of doxorubicin (p-DOX) for cancer imaging and therapy, respectively (Fig. 1c, d). H_2S–PTC–PEG is encapsulated p-Cy to form a nanoprobe ($SNP_{p\text{-}Cy}$) that enabled ultrasensitive detection of various subcutaneous tumors and small (<2 mm) orthotopic colorectal, liver, or lung metastatic tumors. Similarly, we develop a H_2S-responsive nanomedicine ($SNP_{p\text{-}DOX}$) with localized H_2S signal amplification by encapsulating the p-DOX in H_2S–PTC–PEG. $SNP_{p\text{-}DOX}$ could enhance the localized prodrug activation and H_2S gas stimulation to overcome multidrug resistance (MDR) and effectively inhibit tumor growth in MCF7/ADR xenograft tumor, breast cancer lung metastasis, and breast cancer patient-derived xenograft (PDX) models.

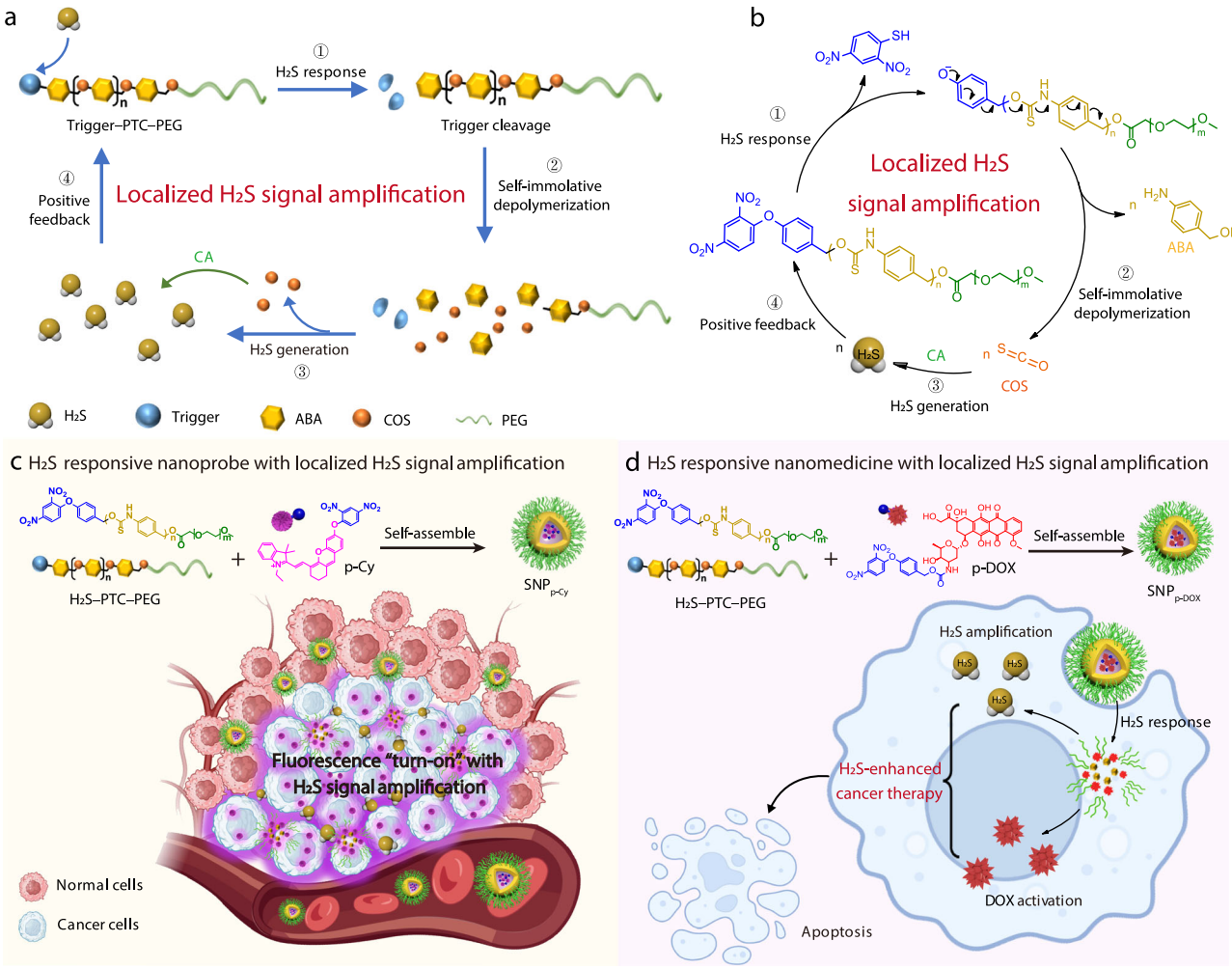

Fig. 1 | Schematic of H_2S-responsive self-immolative poly(thiocarbamate) (PTC) for cancer imaging and therapy. a Illustration of self-immolative PTC following H_2S activation. H_2S-triggered cycle amplification takes advantage of the produced COS, which is then rapidly hydrolyzed to H_2S by CA. ABA: 4-aminobenzyl alcohol, COS: carbonyl sulfide, CA: carbonic anhydrase, PEG: methoxy poly(ethylene glycol). **b** The mechanism of H_2S–PTC–PEG amplification of H_2S signaling. **c** H_2S–PTC–PEG self-assembly into nanoparticles with the encapsulation of the H_2S-responsive fluorescent probe based on hemicyanine dye (p-Cy) to obtain a nanoprobe ($SNP_{p\text{-}Cy}$) for the ultrasensitive tumor imaging. **d** H_2S-responsive anticancer prodrug of doxorubicin (p-DOX) encapsulation into H_2S–PTC–PEG produces a H_2S-responsive nanomedicine ($SNP_{p\text{-}DOX}$) with localized H_2S signal amplification for enhanced cancer therapy. Figures 1c and 1d, created with BioRender.com, were released under a Creative Commons Attribution-NonCommercial-NoDerivs 4.0 International license.

Results

Preparation and characterization of self-immolative PTC

To synthesize the self-immolative PTC, we prepared a monomer that contained aryl isothiocyanate and benzyl alcohol functional groups (compound **1**, Supplementary Fig. 1) that will undergo polyaddition in the presence of di-*n*-butyltin dilaurate (DBTDL). At this point in the polymerization, (4-(2,4-dinitrophenoxy) phenyl) methanol (compound **2**), *p*-methyl-benzylalcohol, or 2-nitrobenzyl alcohol was added as an end-capping reagent to afford the H_2S-triggered (H_2S–PTC), no-trigger PTC (Ctrl–PTC), or UV light-triggered PTC (UV–PTC), respectively. The obtained polymers and intermediates were confirmed via ^{1}H nuclear magnetic resonance (NMR) spectroscopy (Supplementary Fig. 2–8). Gel permeation chromatography (GPC) studies of polymers are shown in Fig. 2a and Supplementary Fig. 15.

To study the H_2S-induced depolymerization of H_2S–PTC, ^{1}H NMR spectroscopy was used to monitor the formation of 4-aminobenzyl alcohol (ABA), the primary by-product of H_2S–PTC depolymerization. As time increased, the broad heteroatomic peak attributed to the H_2S–PTC-repeating unit proton (peak a, b, and c) decreased while the aromatic doublets (peak d and e) peak of ABA appeared (Supplementary Fig. 16 and Fig. 2b). Conversely, the ^{1}H NMR spectra of Ctrl–PTC remain unchanged after incubation with NaHS (10 eq, H_2S donor) over time (Supplementary Fig. 17). Considering the toxicity and stability of H_2S, we substituted sulfide salts (NaHS) for H_2S[46]. The results showed that the chain cleavage of H_2S–PTC was clearly H_2S-responsive.

To test our hypothesis that PTC could release multiple equivalents of H_2S per triggering event, we investigated the H_2S yield of UV–PTC_n with different molecular weights via UV irradiation-induced polymer degradation. Lower molecular weights produced more rapid H_2S production, and the H_2S yields for all PTC with different molecular weights were >85% at 400 min (Fig. 2c and Supplementary Fig. 18). We then used GPC to analyze the remaining polymer fractions of H_2S–PTC (with UV–PTC fraction in the range of 0.1 – 10 wt %) without or with UV irradiation in the presence of CA to hydrolyze COS to H_2S. The sigmoidal degradation curve was indicative of the self-amplifying cascade degradation course (Fig. 2d). More importantly, when UV–PTC was as low as 1 wt %, the H_2S–PTC could still be completely degraded, which was due to UV–PTC releasing multiple equivalents of H_2S following UV-triggered degradation. These findings validate that PTC could release multiple H_2S equivalents during each triggering event.

H_2S-triggered selective degradation of nanoparticles

We then conjugated mPEG–COOH onto the terminal chain of H_2S–PTC to acquire the amphiphilic polymer (H_2S–PTC–PEG, Supplementary Fig. 19), which could self-assemble into nanoparticles (SNP); we also prepared inSNP formed by the non-triggering polymer (Ctrl–PTC–PEG) as a comparison. We used dynamic light scattering (DLS) and transmission electron microscopy (TEM) to examine the H_2S-triggered degradation of SNP because the H_2S-triggered self-immolative degradation process of PTC was accompanied by shrinkage of the nanoparticles. After incubation with NaHS, the intensity-average hydrodynamic diameters (D_h) of SNP continued to decrease, whereas inSNP showed negligible changes (Fig. 2e). Most importantly, the selectivity of SNP was maintained even when over physiological concentrations of GSH (100 mM) were added. Furthermore, we also demonstrated that the response of SNP for H_2S is remained in the presence of GSH (Supplementary Fig. 20). Due to SNP containing the H_2S-responsive endcaps and benzyl thiocarbamates as the repeat unit, H_2S–PTC would undergo cascade degradation through the H_2S stimuli then released COS, ABA (the primary by-product) and PEG. Hence, TEM analysis was used to further assess the H_2S-triggered degradation of SNP. As shown in Fig. 2f, the diameter of SNP remained at 110 nm after incubation without NaHS and showed that SNP had good uniformity and dispersibility. Whereas SNP transformed into small fragments and the size of SNP remarkably decreased to approximately 16 nm after incubation with NaHS in the presence of CA, owing to H_2S-triggered release of the small molecule COS, ABA, hydrophilic polymer PEG and subsequent dissociation of the SNP nanoparticles. These findings indicate that the structure of the nanoparticles completely collapsed, as a result of H_2S–PTC degradation induced by H_2S.

To further investigate the H_2S-triggered self-amplified disintegration of SNP, we used high-performance liquid chromatography (HPLC) to measure the release profile of ABA. In the presence of CA, when the amount of NaHS was reduced to 0.1 eq., the release of ABA increased over time and reached the same level as that of 10 eq. at 12 h (Fig. 2g). However, in the absence of CA, both the 0.1 and 1 eq. NaHS concentrations had low ABA release rates over the identical period. This demonstrated that H_2S-triggered cycle amplification was achieved by exploiting the generated COS, which was promptly converted into H_2S by CA, producing a self-amplifying backbone degradation cascade and disintegration of the SNP.

Preparation of $SNP_{p\text{-}Cy}$ as a H_2S-responsive nanoprobe for ultrasensitive tumor image

We employed a H_2S-responsive fluorescent probe based on hemicyanine dye (p-Cy) (Supplementary Fig. 9–11) to fabricate nanoprobes ($SNP_{p\text{-}Cy}$) by doping it into SNP. $SNP_{p\text{-}Cy}$ would specifically amplify H_2S signals at the tumor sites and selectively activate p-Cy under the stimulation of H_2S, leading to near-infrared (NIR) fluorescence turn-on (Fig. 3a). First, we investigated the response of p-Cy to H_2S by incubating p-Cy with NaHS in phosphate-buffered saline (PBS). As shown in Supplementary Fig. 21a, p-Cy showed an absorption peak at 590 nm and exhibited a violet color, which appeared as a new peak at 705 nm and changed to a sapphire color after adding NaHS. The fluorescence spectra of p-Cy in the absence and presence of NaHS is shown in Supplementary Fig. 21b, upon the addition of NaHS, a 27-fold enhancement of the fluorescence intensity was observed. Moreover, as the incubation time or NaHS concentration increased, the fluorescence intensity of p-Cy increased steadily (Supplementary Fig. 21c, d).

Subsequently, we investigated the sensitivity of $SNP_{p\text{-}Cy}$ toward H_2S. The fluorescence intensity of $SNP_{p\text{-}Cy}$ gradually increased as the concentration of NaHS increased (Fig. 2h). The limit of detection (LOD) for H_2S was obtained in buffer solution and was 0.02 μM (3σ/k) for $SNP_{p\text{-}Cy}$, which was 7-fold lower that the LOD for p-Cy (Fig. 2i). Moreover, the fluorescence signal of $SNP_{p\text{-}Cy}$ was much higher than that of p-Cy at 0.1 eq. NaHS (Fig. 2j). We attribute these results to $SNP_{p\text{-}Cy}$ degrading in an exponential cascade and subsequently releasing large amounts of H_2S, thereby amplifying the fluorescence signal in a short period.

To determine the selectivity and specificity of $SNP_{p\text{-}Cy}$ toward H_2S, we selected various possible competitive relevant analytes, including 100 μM NaHS, PBS buffer, and other species, including cations (K^+, Ca^{2+}, Na^+, 1 mM), anions (SO_4^{2-}, SO_3^{2-}, HSO_3^-, $S_2O_3^{2-}$, SCN^-, NO_3^-, NO_2^-, CO_3^{2-}, HCO_3^{2-}, 1 mM), reactive oxygen species (H_2O_2, ClO^-, $ONOO^-$, $^1O_2$, 1 mM), reductant (L-Cys: L-cysteine, Hcy: homocysteine, MAA: mercaptoacetic acid, SBS: sodium benzenesulfinate, VC: ascorbic acid, DTT: dithiothreitol 1 mM; GSH: glutathione, 10 mM). Of these, only NaHS promoted an apparent fluorescence enhancement, indicating $SNP_{p\text{-}Cy}$ showed high selectivity for H_2S in vitro (Fig. 3b).

Fluorescence imaging in living cells

We next sought to investigate the capability of $SNP_{p\text{-}Cy}$ for fluorescence imaging in living cells. Since the tumor microenvironment is more H_2S-abundant than healthy tissues, we tested the specificity of $SNP_{p\text{-}Cy}$ activation by evaluating CT26 as H_2S-rich cancer cells, Hepa 1-6 as H_2S-deficient cancer cells, and L929 fibroblast normal cells. Cells were incubated with NIR hemicyanine dye (CyOH), p-Cy, $SNP_{p\text{-}Cy}$, or $inSNP_{p\text{-}Cy}$ for 4 h and then examined by confocal laser scanning microscopy (CLSM). $SNP_{p\text{-}Cy}$ produced sufficient fluorescence

https://doi.org/10.1038/s41467-024-52006-0

a

Entries	Sample	Triggers	DP[a]	M_n (kDa)[a]	M_n (kDa)[b]	PDI[b]
P_1	UV–PTC_6	UV light	6	1.1	1.2	1.41
P_2	UV–PTC_{11}	UV light	11	2.0	2.1	1.24
P_3	UV–PTC_{17}	UV light	17	3.1	3.3	1.28
P_4	H_2S–PTC_{11}	H_2S	11	2.1	2.3	1.25
P_5	Ctrl–PTC_{11}	——	11	2.0	2.0	1.58
PP_1	H_2S–PTC_{11}–PEG	H_2S	——	4.2	4.0	1.23
PP_2	Ctrl–PTC_{11}–PEG	——	——	4.1	4.1	1.44

[a] Calculated from ^{1}H NMR spectra.
[b] Determined by GPC with polystyrene standardsin (eluent: THF, 1 mL min^{-1}).

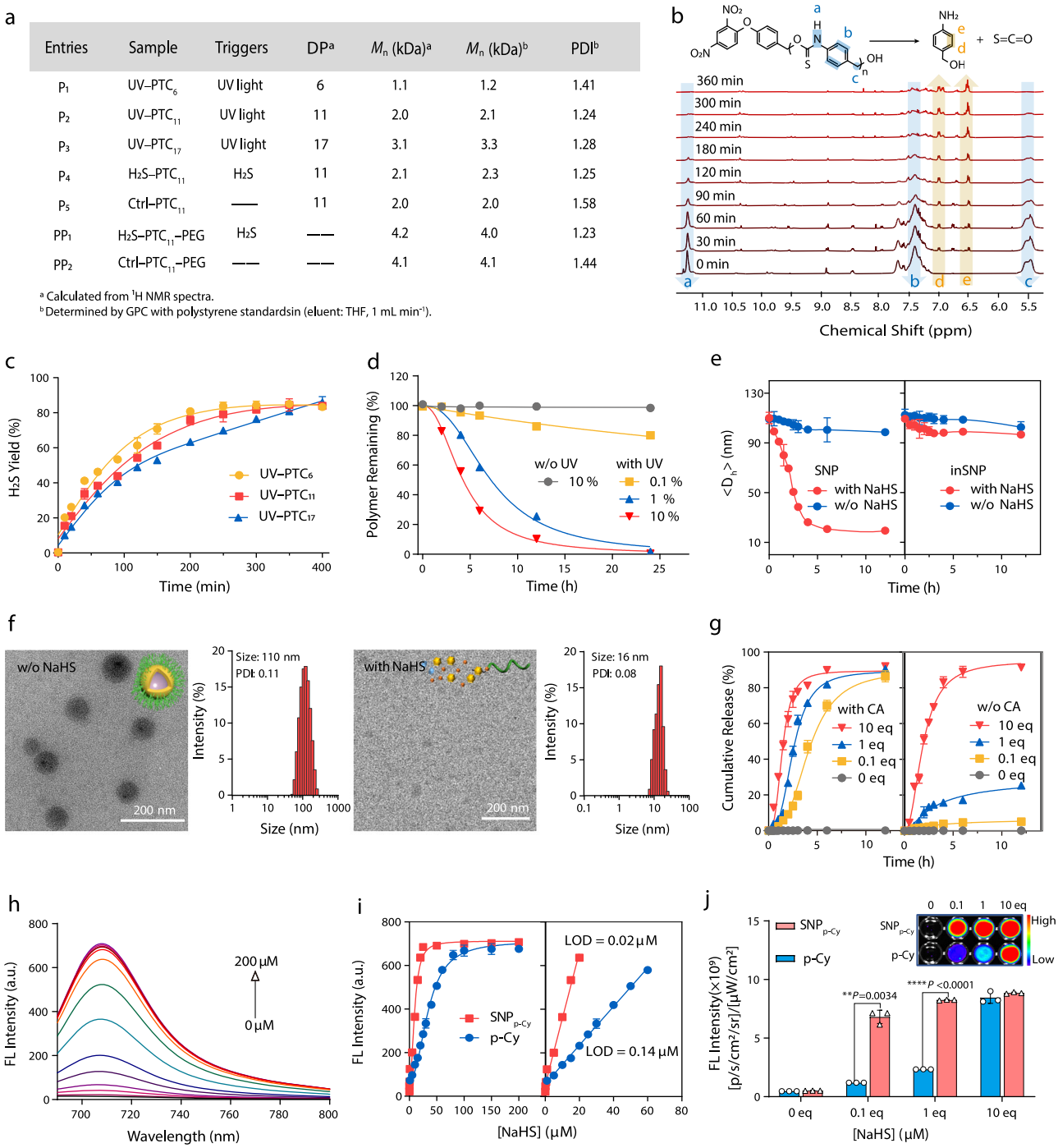

Fig. 2 | Preparation and characterization of self-immolative PTC. **a** Characterization of polymers. DP: degree of polymerization, M_n: number averaged molecular weights of polymer, PDI: polydispersity index, M_w/M_n. **b** ^{1}H NMR degradation study of H_2S–PTC after incubation with NaHS for different times. **c** H_2S generation curves of UV–PTC_6, UV–PTC_{11} and UV–PTC_{17} with UV irradiation in the presence of CA. **d** The fraction of remaining polymers of H_2S–PTC (total concentration 1.0 mg mL^{-1}, with UV–PTC fraction in the range 0.1–10 wt %) without and with UV irradiation (365 nm) in the presence of CA. **e** Evolution of D_h recorded for SNP and inSNP nanoparticles after incubation with NaHS in the presence of CA for different times. **f** Particle size and TEM image of SNP with and without NaHS in the presence of CA (Experiments were repeated three times). **g** Cumulative ABA release profile of SNP after being treated with various NaHS concentrations (0, 0.1, 1, and 10 eq) in the presence or absence of CA. **h** Fluorescence spectra of $SNP_{p\text{-}Cy}$ after incubation with different concentrations of NaHS in the presence of CA. **i** The fluorescence intensity changes of $SNP_{p\text{-}Cy}$ and p-Cy after incubation with different concentrations of NaHS in the presence of CA, and the linear response at lower concentrations. **j** Fluorescence images and intensity analysis of $SNP_{p\text{-}Cy}$ and p-Cy after being treated with various NaHS concentration (0, 0.1, 1, and 10 eq) in the presence of CA. Data are presented as the mean ± s.d. (n = 3 independent samples). Statistical differences were analyzed by Student's t test (two tails). $^{**}P < 0.01$, $^{****}P < 0.0001$. Source data are provided as a Source Data file.

https://doi.org/10.1038/s41467-024-52006-0

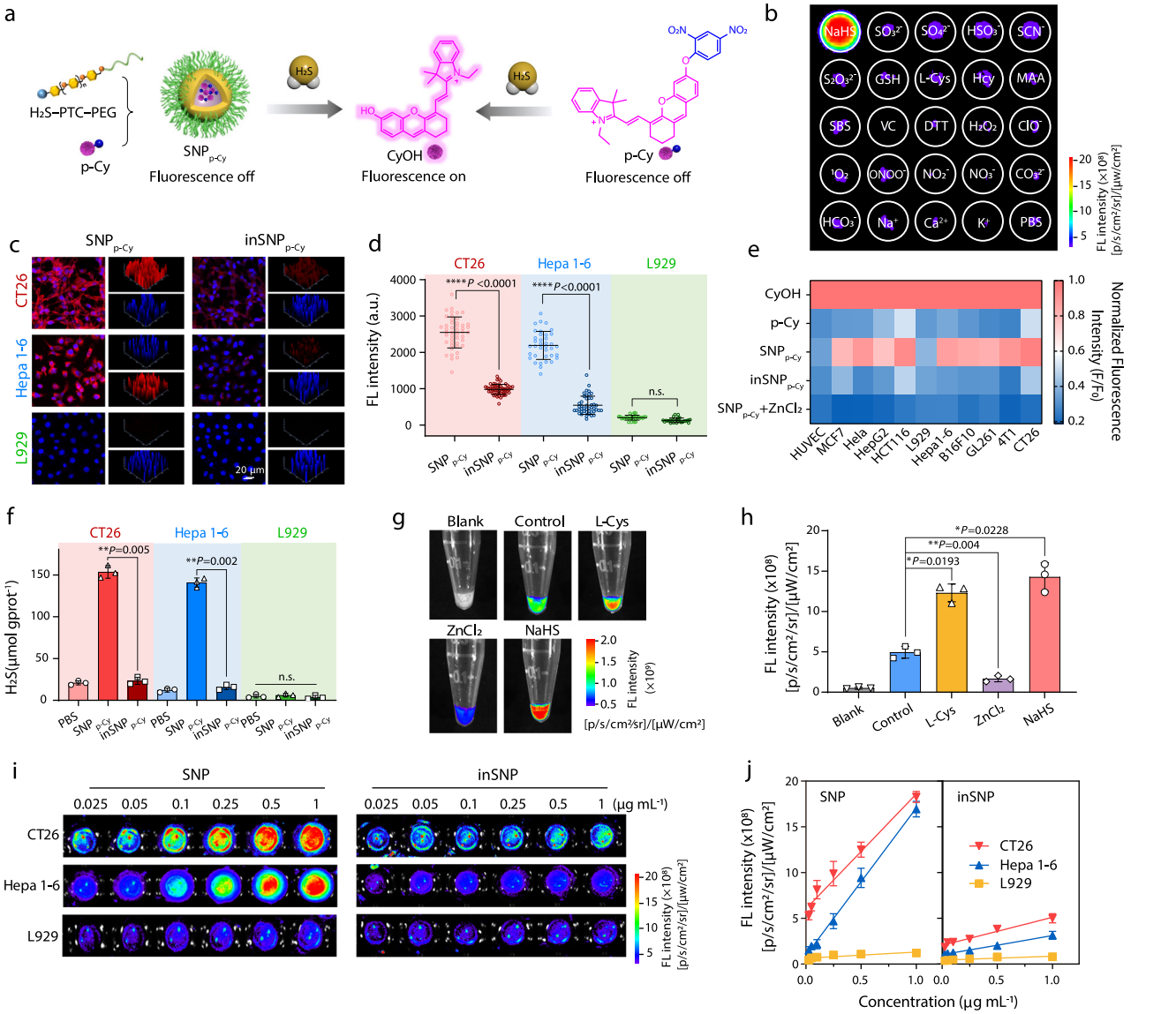

Fig. 3 | Preparation of $SNP_{p\text{-}Cy}$ for fluorescence imaging in living cells. **a** Schematic for the preparation of $SNP_{p\text{-}Cy}$ and the fluorescence "turn-on" after H_2S response. **b** Fluorescence images of $SNP_{p\text{-}Cy}$ upon incubation with various relevant analytes, including NaHS, PBS buffer, and other species such as cations, anions, reactive oxygen species, and reductants. **c** Representative fluorescence microscopy images of CT26, Hepa 1-6, and L929 cells incubated with $SNP_{p\text{-}Cy}$ or $inSNP_{p\text{-}Cy}$ (Experiments were repeated three times). Blue: Hoechst 33342 (bound to DNA in cell nuclei), red: CyOH. **d** Quantification of the fluorescence signal of the single cell in **c**. **e** Heat map shows the normalized fluorescence intensity in various cells after incubated with CyOH, p-Cy, $SNP_{p\text{-}Cy}$, $inSNP_{p\text{-}Cy}$ and $SNP_{p\text{-}Cy}$ together with 300 μM $ZnCl_2$. **f** H_2S-generating ability assessed. **g** Fluorescence imaging and intensities **h** of CT26 cells pellets incubated with $SNP_{p\text{-}Cy}$ (4 μg mL^{-1}) together with 300 μM $ZnCl_2$ (incubation in advance for 10 min), 1 mM NaHS (incubation in advance for 1 h), and 200 μM L-Cys (incubation in advance for 1 h); blank: untreated cells; control: only $SNP_{p\text{-}Cy}$ (4 μg mL^{-1}) treated cells. **i** Fluorescence images of CT26, Hepa 1-6 and L929 cells upon co-incubation p-Cy (4 μg mL^{-1}) with varying concentrations of SNP or inSNP (0.025, 0.05, 0.1, 0.25, 0.5 and 1 μg mL^{-1}). **j** Plot of the fluorescence intensity of p-Cy and the concentration of SNP or inSNP from 0.025 to 1 μg mL^{-1}. Data denote mean ± s.d. (n = 3 independent samples). Statistical differences were analyzed by Student's *t*-test (two tails). $^*P < 0.05$, $^{**}P < 0.01$, $^{****}P < 0.0001$, n.s., no significant difference. Source data are provided as a Source Data file.

activation in both tumor cell lines compared with that in normal cells (Fig. 3c, d and Supplementary Fig. 22); conversely, none of the negative control group (p-Cy and $inSNP_{p\text{-}Cy}$) was activated in either cell type. Furthermore, $SNP_{p\text{-}Cy}$ showed highly selective fluorescence activation against various cancer cells, with minimal fluorescence activation against normal cells (Fig. 3e). To confirm that the fluorescence enhancement was specifically activated by H_2S, the endogenous H_2S level was detected in living cells after different treatments. As expected, the H_2S levels in $SNP_{p\text{-}Cy}$-treated tumor cells was significantly increased, whereas the H_2S levels in cells treated with $inSNP_{p\text{-}Cy}$ were almost unchanged (Fig. 3f and Supplementary Fig. 23). Next, we verified the capability of SNP to amplify the H_2S signal. The fluorescence intensity of p-Cy was positively correlated with the concentration of SNP from 0.025 to 1 μg mL^{-1} in cancer cells (CT26 and Hepa 1-6) (Fig. 3i, j). Conversely, the fluorescence of p-Cy was hardly activated by inSNP in all tested cells. Together, these results suggest that $SNP_{p\text{-}Cy}$ was only activated in tumor cells as these have relatively higher levels of H_2S to induce self-immolative degradation of PTC accompanied by amplification of the endogenous H_2S signal.

We subsequently applied $SNP_{p\text{-}Cy}$ to track the fluctuation of H_2S in CT26 cells (Fig. 3g, h). The fluorescence signal in the CT26 cell pellet after treatment with $SNP_{p\text{-}Cy}$ was substantially reduced when pre-treated with $ZnCl_2$ to scavenge H_2S. Furthermore, incubation of CT26 cells with L-Cys (a precursor of H_2S biosynthesis) or NaHS (extraneous

H_2S donor) to upregulate intracellular H_2S levels could augment the fluorescence intensity, demonstrating that $SNP_{p\text{-}Cy}$ was a specific probe for H_2S.

Fluorescence imaging of $SNP_{p\text{-}Cy}$ in different subcutaneous cancer models

$SNP_{p\text{-}Cy}$ exhibited high sensitivity and specificity toward H_2S in living cells and therefore holds considerable potential in precise cancer imaging. Hence, we performed fluorescence imaging and distribution analysis of $SNP_{p\text{-}Cy}$ or $inSNP_{p\text{-}Cy}$ in five animal tumor models, including multifarious subcutaneous cancers (colon, brain, breast, and liver) and PDX colorectal carcinoma model. The fluorescence signal of $SNP_{p\text{-}Cy}$ in tumor tissues was continuously enhanced within 12 h of postinjection in all five tumor models, whereas none of the tumor models observed fluorescence activation in $inSNP_{p\text{-}Cy}$ treated group (Fig. 4a and Supplementary Fig. 24, 25). A heat map showed the heterogeneity of $SNP_{p\text{-}Cy}$ fluorescence activation in different tumor types (Fig. 4b). Fluorescence imaging of excised organs demonstrated that $SNP_{p\text{-}Cy}$ fluorescence activation occurred more significantly in tumor tissue than in other organs (Supplementary Fig. 26).

Fluorescence imaging of orthotopic liver tumors in mice

Nanoparticles are often present in high concentrations in the liver, which would hinder hepatoma imaging; therefore, we constructed an orthotopic liver tumor model to determine if $SNP_{p\text{-}Cy}$ could sensitively identify tumors. Fluorescence activation was observed in all different sizes of orthotopic liver tumor sites, providing an excellent imaging contrast between the tumor and surrounding liver tissue (Fig. 4c, d and Supplementary Fig. 27). The fluorescence signal of tumor was 5-fold that in the around liver tissue (Fig. 4e and Supplementary Fig. 28).

$SNP_{p\text{-}Cy}$ and $inSNP_{p\text{-}Cy}$ were consequently used in orthotopic liver tumor resection to verify whether the nanoprobe could accurately delineate tumor margins. The orthotopic liver tumor could be clearly observed without background interference in $SNP_{p\text{-}Cy}$ group (Fig. 4f), which was consistent with bioluminescence; the tumor site and healthy liver can be clearly distinguished by the fluorescence signal of $SNP_{p\text{-}Cy}$. Furthermore, the fluorescence signal of tumor site increased steadily and reached a maximum intensity at 12 h after injection (Fig. 4g, h). The signal-to-background ratio (SBR) of fluorescence of $inSNP_{p\text{-}Cy}$ was low, which significantly increased to 13.13 ± 1.78 in $SNP_{p\text{-}Cy}$-treated mice (Fig. 4i). Therefore, ultrasensitive imaging achieved by $SNP_{p\text{-}Cy}$ enabled tumor tissue to be distinguished from surrounding liver tissue.

Detection of lung cancer metastasis by $SNP_{p\text{-}Cy}$

To showcase the capability of nanoprobes in identifying small metastatic carcinomas, we assessed $SNP_{p\text{-}Cy}$ in a model of metastatic lung cancer. Due to tumor microenvironment is more H_2S-abundant than that of healthy tissues (Supplementary Fig. 29), which naturally endowed H2S − PTC with tumor-specific H_2S release. Subsequently, the released COS is promptly hydrolyzed to H_2S by the widely present CA (Supplementary Fig. 30), enabling the endogenous H_2S signal to be rapidly amplified. Hence, $SNP_{p\text{-}Cy}$ could identify the majority of lung metastases tumors, and even those with a diameter <1 mm (Fig. 4j, k). Furthermore, $SNP_{p\text{-}Cy}$ produced a significantly stronger fluorescence signal than $inSNP_{p\text{-}Cy}$ (Fig. 4l) and displayed better SBR than $inSNP_{p\text{-}Cy}$ (Fig. 4m). Thus, $SNP_{p\text{-}Cy}$ could offer a high SBR to clearly define small metastatic cancer via fluorescence imaging.

In vivo fluorescence imaging in orthotopic model of colorectal cancer

We also performed experiments using orthotopic colorectal cancer models because of the high levels of H_2S found in colorectal cancer. $SNP_{p\text{-}Cy}$ clearly revealed small colorectal tumors while barely detectable fluorescence was observed in other tissues (Fig. 4n, p). Interestingly, the fluorescence imaging of $SNP_{p\text{-}Cy}$ revealed the presence of small (~2 mm) colorectal tumors that had escaped detection via $inSNP_{p\text{-}Cy}$, with an SBR of $SNP_{p\text{-}Cy}$ of up to 14.4 ± 2.03 (Fig. 4o). Thus, the fluorescence of $SNP_{p\text{-}Cy}$ preferentially recovers in tumor sites, rather than in noncancerous tissues.

$SNP_{p\text{-}DOX}$ boosts intracellular H_2S and overcomes MDR

H_2S has been demonstrated to induce acute toxicity through inhibition of mitochondrial cytochrome c oxidase (COX IV) activity[47,48]. Once the activity of COX IV is inhibited, adenosine triphosphate (ATP) production will sharply decrease and lead to efflux pump dysfunction to overcome MDR (Fig. 5a). Therefore, we developed a H_2S-responsive nanomedicine with localized H_2S signal amplification ($SNP_{p\text{-}DOX}$) by encapsulating the H_2S-responsive anticancer prodrug of doxorubicin (p-DOX, Supplementary Fig. 12–14) in the amphiphilic polymer H_2S–PTC–PEG. The drug-loading efficiencies (DLEs) of $SNP_{p\text{-}DOX}$ and $SNP_{p\text{-}DOX}$ were 35.7% and 31.4%, and the drug-loading contents (DLCs) were 5.1% and 4.5%, respectively, which were determined by UV absorption of the microplate system at 480 nm. The intracellular H_2S concentration in MCF7/ADR cells after different treatments was first determined to confirm that $SNP_{p\text{-}DOX}$ enabled the elevation of H_2S. $SNP_{p\text{-}DOX}$ could significantly promote the production of endogenous H_2S compared with that in the PBS group (Fig. 5b). We also investigated the endogenous H_2S level in living cells by using a commercially available H_2S probe (Washington State Probe-1, WSP-1). WSP-1 is a non-fluorescent probe after internalized by cells, which could rapidly react with H_2S and selectively turn on fluorescence. As shown in Supplementary Fig. 31, strong fluorescence was observed in MCF7/ADR cells after being treated with SNP. However, after adding H_2S scavenger $ZnCl_2$, cells treated with SNP only exhibited a weak fluorescence signal. The above results confirmed the H_2S-generating capacity of SNP. To determine whether the elevation of H_2S induced by $SNP_{p\text{-}DOX}$ could disrupt mitochondrial function, we used the 6-tetrachloro-1,1,3,3-tetraethyl-imidacarbocyanine iodide (JC-1) assay to monitor the alteration in mitochondrial membrane potential (MMP). JC-1 aggregation in mitochondria produces red fluorescent J-aggregates, whereas when the MMP decreases, this fluorescence transitions from red to green. Both PBS and inSNP-treated MCF7/ADR cells exhibited pronounced red fluorescence within the mitochondria (JC-1 aggregates), suggesting good mitochondrial integrity (Fig. 5c and Supplementary Fig. 32), whereas SNP-treated cells exhibited strong green fluorescence (JC-1 monomers), indicating that the mitochondrial membrane had been damaged. Furthermore, we used an extracellular flux analyzer to measure the cellular oxygen consumption rate (OCR, an indicator of mitochondrial respiration) of MCF7/ADR cells after different treatments. As expected, significant inhibition of OCR was observed for the cells treated with $SNP_{p\text{-}DOX}$, and adversely impacted many major bioenergetics parameters, such as basal respiration, maximal respiration, and ATP synthesis (Fig. 5d). Thus, SNP could cause mitochondrial dysfunction by amplifying the H_2S signal in MCF7/ADR cells.

To explore the mechanism of endogenous H_2S elevation in overcoming MDR, we analyzed the expression of COX IV and P-glycoprotein (P-gp) in MCF7/ADR cells via western blotting (WB). Compared with that in other groups, the expression of COX IV and P-gp in the treatment group of $SNP_{p\text{-}DOX}$ was markedly inhibited (Fig. 5e, f, h and Supplementary Fig. 33). We then stained P-gp with Alexa Fluor®488 conjugated antimouse antibody to ascertain the distribution of P-gp following $SNP_{p\text{-}DOX}$ treatment. The majority of P-gp efflux pumps in both the PBS and $inSNP_{p\text{-}DOX}$ groups were distributed on cytomembrane while most of the P-gp in the $SNP_{p\text{-}DOX}$ group was found in the cytoplasm (Fig. 5g). This phenomenon may be caused by the disruption of mitochondrial function, leading to a lack of ATP supply and disruption of P-gp efflux pump transportation to the cytomembrane. Together, these results indicate that $SNP_{p\text{-}DOX}$-induced H_2S elevation can cause mitochondrial dysfunction and affect P-gp function.

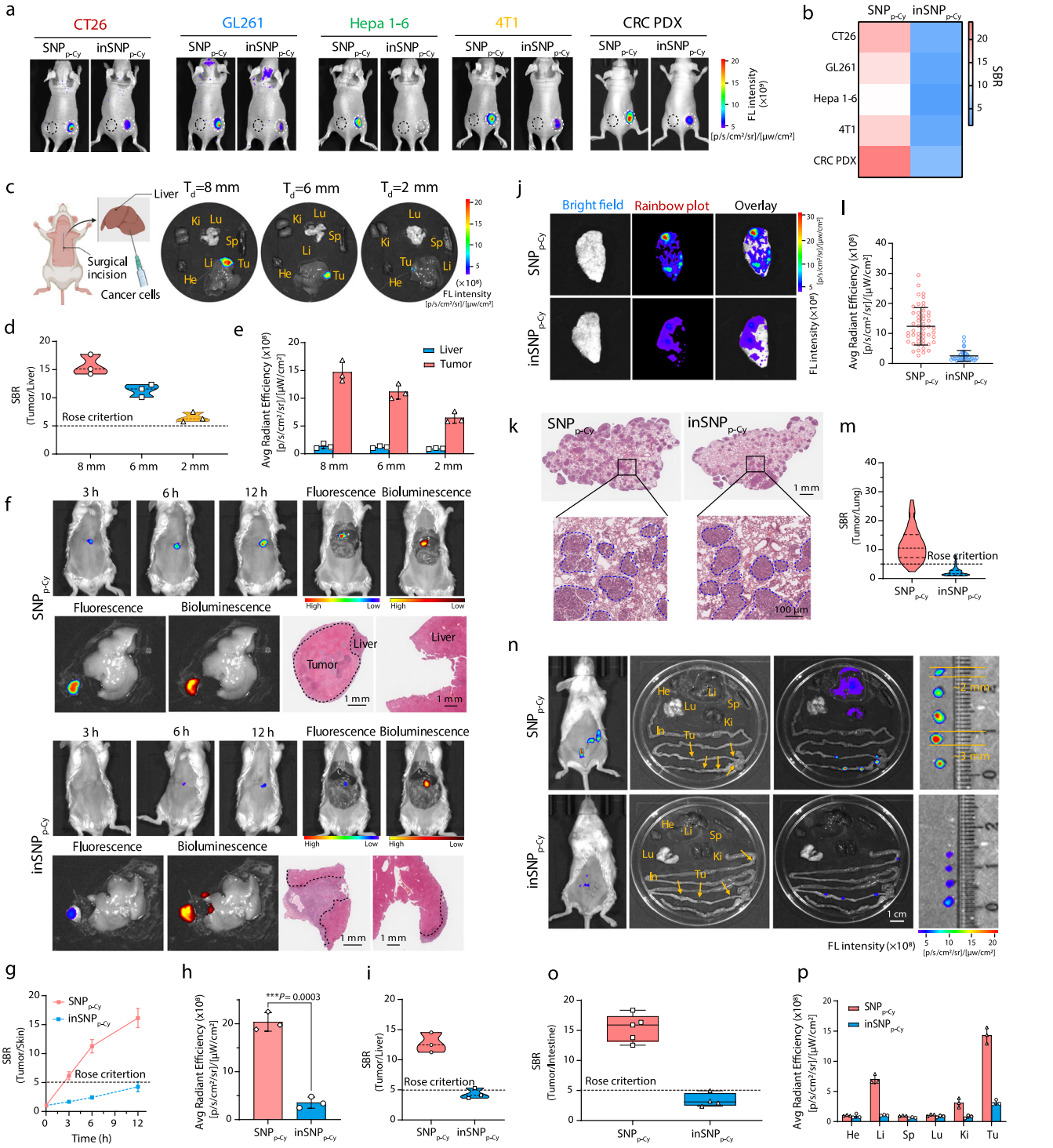

We then quantified the DOX efflux ratio by flow cytometry and assessed the DOX uptake by CLSM imaging and HPLC. Following $SNP_{p\text{-}DOX}$ treatment, the DOX efflux rate was reduced to 20.85 ± 2.11% whereas this reached 71.62 ± 3.04% when incubated with DOX (Fig. 5i). Analogously, the $SNP_{p\text{-}DOX}$ group exhibited a greater red fluorescence intensity of DOX than either the free DOX or $inSNP_{p\text{-}DOX}$ groups in MCF7/ADR cells (Fig. 5j). The cellular uptake of DOX after different treatments was quantitatively analyzed by HPLC. In MCF7/ADR cells, the $SNP_{p\text{-}DOX}$ group showed higher DOX internalization than that in cells treated with free DOX and $inSNP_{p\text{-}DOX}$ (Supplementary Fig. 34). These results confirmed that the elevated H_2S could effectively restrain the P-gp function in MCF7/ADR cells when incubated with $SNP_{p\text{-}DOX}$ so that the DOX efflux ratio was decreased and DOX uptake increased.

We used the methylthiazolyldiphenyl-tetrazolium bromide (MTT) assay to assess the in vitro cytotoxicity of free drugs (DOX and p-DOX) or nanoparticles ($SNP_{p\text{-}DOX}$ and $inSNP_{p\text{-}DOX}$) against MCF7 cells, doxorubicin-resistant cells (MCF7/ADR), and epithelial cells (HUVECs). The cytotoxicity of p-DOX toward MCF7, MCF7/ADR, and HUVEC cells was significantly reduced compared with that of DOX (Supplementary Fig. 35). Conversely, $SNP_{p\text{-}DOX}$ could efficiently kill both MCF7 and MCF7/ADR cells, even though free DOX had low cytotoxicity to MCF7/ADR cells. Intriguingly, the $SNP_{p\text{-}DOX}$ also showed low cytotoxicity in the normal cell type (HUVECs) (Fig. 5k). H_2S generated by PTC would

Fig. 4 | Fluorescence imaging in vivo. a The fluorescence images in five different tumor models (colon, brain, liver, breast, and PDX colorectal cancers). White circles represent tumors, black circles represent normal tissues. **b** Heat map shows the SBR in various tumor models at 12 h post-injection of $SNP_{p\text{-}Cy}$ or $inSNP_{p\text{-}Cy}$. **c** Representative ex vivo fluorescence images of main organs (e.g., liver (Li), lung (Lu), heart (He), kidneys (Ki), spleen (Sp), and tumor (Tu)) resected from orthotopic Hepa 1-6 tumor-bearing mice at 12 h post *i.v.* injection of $SNP_{p\text{-}Cy}$. **d** Comparison of the SBRs for fluorescence imaging in different sizes of orthotopic liver tumors. **e** Comparison of the average fluorescence intensities of different-sized tumors. **f** In vivo and ex vivo fluorescence images of orthotopic Hepa 1-6 tumor-bearing mice after *i.v.* injection of the $SNP_{p\text{-}Cy}$ or $inSNP_{p\text{-}Cy}$ at different time points. **g** Comparison of the SBRs for fluorescence signals in mice over time. Quantification of the average fluorescence intensities **h** and SBR **i** of tumors following indicated treatments. **j** Representative bright-field, rainbow plot (fluorescence imaging) and overlay images of resected lungs bearing metastases 12 h after *i.v.* injection of $SNP_{p\text{-}Cy}$ or $inSNP_{p\text{-}Cy}$ (n = 3 mice per group). **k** Representative H&E staining of sections from imaged lungs bearing metastases. Quantification of the average fluorescence intensities **l** and SBR **m** of the representative image from one of three independent fields of lungs metastases tumors. **n** The in vivo and ex vivo fluorescence images of orthotopic colorectal tumors after *i.v.* injection of $SNP_{p\text{-}Cy}$ or $inSNP_{p\text{-}Cy}$ (n = 3 mice per group). Quantification of the SBR **o** and average fluorescence intensities **p** of the representative image from one of three independent fields of colorectal tumors. The box plot shows the 25th percentile, the median, the 75th percentile, and minimum/maximum whiskers. Data denote mean ± s.d. (n = 3 independent samples). Statistical differences were analyzed by Student's *t*-test (two tails). $^{***}P < 0.001$. Source data are provided as a Source Data file. Figure 4c, created with BioRender.com, was released under a Creative Commons Attribution-NonCommercial-NoDerivs 4.0 International license.

damage mitochondria, and produce partial toxicity to cells. Therefore, we investigated the survival ability of MCF7, MCF7/ADR, and HUVEC cells after incubation with various concentrations of SNP and inSNP without DOX loading (Supplementary Fig. 36), which showed less toxicity to cells. In addition, the apoptosis in MCF7/ADR cells was detected by an Annexin V-FITC/7-AAD flow cytometry assay. As shown in Supplementary Fig. 37-39, cells treated with $SNP_{p\text{-}DOX}$ exhibited the highest pro-apoptosis rate (16.5 ± 0.72%), and the total apoptotic rates (including early and late apoptotic rates) were as high as 43.94 ± 2.81%. Overall, $SNP_{p\text{-}DOX}$ could selectively activate the prodrug and overcome MDR through upregulating of intracellular H_2S levels in cancer cells.

Activation of H_2S-responsive prodrug in tumor-bearing mice

Mice bearing MCF7/ADR tumor xenografts were established, and free DOX, $SNP_{p\text{-}DOX}$, or $inSNP_{p\text{-}DOX}$ were intravenously injected into these mice. At 12 h postinjection, tumor and major organs were collected, and the concentration of DOX was quantified via HPLC analysis (Fig. 5l). The DOX content in the tumor tissue of $SNP_{p\text{-}DOX}$ group was higher than that of free DOX and $inSNP_{p\text{-}DOX}$ groups, and most of drugs in the $inSNP_{p\text{-}DOX}$ group existed as nonactivated prodrugs (Fig. 5m, n). In addition, intravenously administered free DOX was predominantly found in the heart and metabolic organs such as the liver and kidney, whereas the $SNP_{p\text{-}DOX}$ group exhibited lower DOX contents in the other organs (Supplementary Fig. 40). Collectively, these results indicated that $SNP_{p\text{-}DOX}$ can enhance localized prodrug activation. Following intravenous injections of PBS, $SNP_{p\text{-}DOX}$, and $inSNP_{p\text{-}DOX}$ in ICR mice and collecting blood samples at various predetermined times, the H_2S concentration was recorded. As displayed in Supplementary Fig. 41a, compared to PBS, $SNP_{p\text{-}DOX}$ only slightly increases the concentration of H_2S in the blood. Furthermore, we analyzed the H_2S concentration after different treatments for 4 h (the time point of the highest H_2S concentration in $SNP_{p\text{-}DOX}$ group), and found that there was no significant difference among all groups (Supplementary Fig. 41b). Collectively, these results indicated that $SNP_{p\text{-}DOX}$ was stable in the physiological context.

Therapy of orthotopic MCF7/ADR tumor by $SNP_{p\text{-}DOX}$

Inspired by the ability of $SNP_{p\text{-}DOX}$ to overcome MDR in cells, we assessed the antitumor efficacy in MCF7/ADR tumor-bearing NOD/SCID mice. Mice were divided into three groups in a random manner ($n = 5$), and treated with PBS, $inSNP_{p\text{-}DOX}$, and $SNP_{p\text{-}DOX}$ (Fig. 6a). Tumor growth in the $inSNP_{p\text{-}DOX}$ group was rapid, a similar trend with PBS group, and the tumor suppression was weak (Fig. 6b, d). Conversely, mice with $SNP_{p\text{-}DOX}$ exhibited prominent tumor growth inhibition (Supplementary Figs. 42 and 43), implying that the upregulation of intracellular H_2S levels in tumors can overcome MDR. In addition, none of the groups exhibited any apparent changes in body weight (Supplementary Fig. 44). To further study the in vivo degradation of $SNP_{p\text{-}DOX}$, the H_2S concentration in tumor, major organs and blood was quantified. As shown in Fig. 6e and Supplementary Fig. 45, administration of $SNP_{p\text{-}DOX}$ exhibited higher H_2S concentration in the tumor tissues, reaching 2.6-fold higher than that of $inSNP_{p\text{-}DOX}$.

Fresh mouse tumor tissue was harvested to assess the changes in COX IV and P-gp expression following different treatments. In comparison with that in the other groups, the expression of COX IV in the $SNP_{p\text{-}DOX}$ treatment group was significantly inhibited and that of P-gp was also reduced (Fig. 6c and Supplementary Fig. 46). Thus, consistent with these findings in cellular studies, $SNP_{p\text{-}DOX}$ also could overcome MDR in vivo.

In vivo antimetastatic effect of $SNP_{p\text{-}DOX}$

To verify the effect of $SNP_{p\text{-}DOX}$ against breast cancer lung metastases, a lung metastasis model was established via tail vein injection of MCF7/ADR cells (Fig. 6f). $SNP_{p\text{-}DOX}$ considerably inhibited metastatic lung tumor growth, resulting in the lowest lung weight (0.34 ± 0.09 g, which is close to the weight of normal lung) among all the treatment groups (Fig. 6g). Representative images and histological hematoxylin and eosin (H&E) staining of lungs harvested at the end of the study verified that the treatment of $SNP_{p\text{-}DOX}$ considerably reduced metastatic nodule formation in the lung (Fig. 6j). The number of metastatic nodules in $SNP_{p\text{-}DOX}$ was 7.9- and 8.6-fold lower than that in the $inSNP_{p\text{-}DOX}$ and PBS groups, respectively (Fig. 6h). Furthermore, the survival analysis confirmed the optimal therapeutic effect of $SNP_{p\text{-}DOX}$, revealing 50% survival of the mice within 35 days, whereas all mice from the other groups died in 26 days (Fig. 6i).

Antitumor capability evaluation via a breast carcinoma (BCa) PDX model

We then established an orthotopically implanted PDX model of breast cancer in NOD/SCID mice to assess the potential clinical application of $SNP_{p\text{-}DOX}$ (Fig. 6k). $SNP_{p\text{-}DOX}$ could markedly inhibit tumor growth, in contrast to $inSNP_{p\text{-}DOX}$ (Fig. 6l and Supplementary Fig. 47–49). Terminal deoxynucleotidyl transferase dUTP nick end labeling (Tunel) assay and H&E staining of tumor sections revealed a significantly greater number of apoptotic cells in the $SNP_{p\text{-}DOX}$ group than in the other sample treatment groups (Supplementary Fig. 50). Overall, our findings revealed that $SNP_{p\text{-}DOX}$ treatment could markedly inhibit tumor growth in the PDX model. Furthermore, there was no obvious change in mouse body weight after the different treatments (Supplementary Fig. 51).

Following the completion of the 32-day therapy, mice were sacrificed, and the major organs were harvested to evaluate the in vivo toxicity of $SNP_{p\text{-}DOX}$. No pathological processes were found with H&E staining of the heart, liver, spleen, lung, or kidney tissues after $SNP_{p\text{-}DOX}$ treatment (Supplementary Fig. 52). Furthermore, we tested the in vivo side effects at 32 days after different treatments. The evaluation of liver function assessed the levels of alanine transaminase (ALT) and aspartate transferase (AST) while kidney function was assessed using blood urea nitrogen (BUN) and blood glucose and blood lipids were assessed using blood glucose (GLU) and cholesterol (CHO), respectively. None of the treatments affected the blood

https://doi.org/10.1038/s41467-024-52006-0

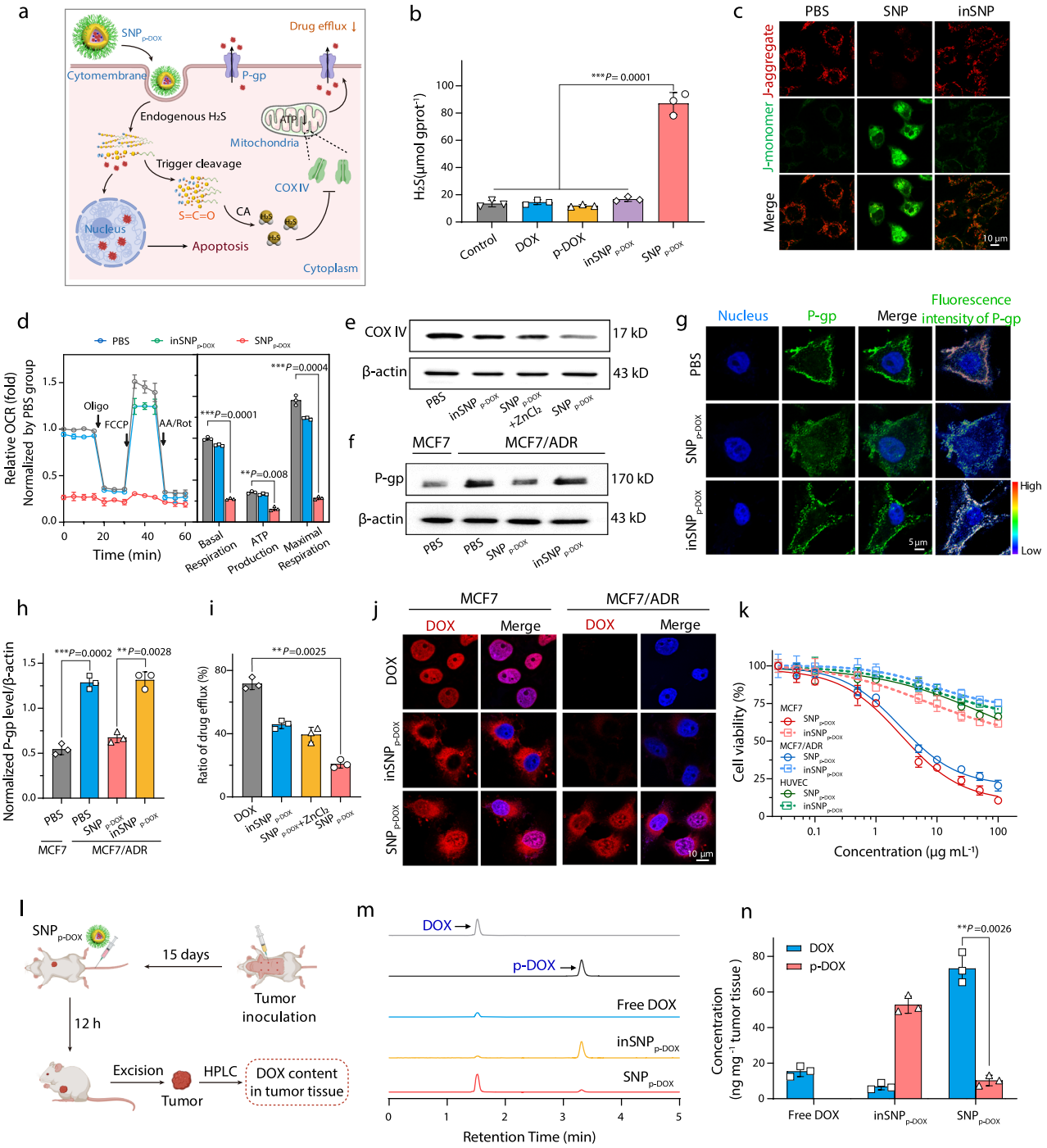

Fig. 5 | SNP$_{p\text{-}DOX}$ induces MCF7/ADR cell death via intracellular H_2S generation. **a** The mechanism on SNP$_{p\text{-}DOX}$ overcoming MDR. **b** H_2S concentration determination of MCF7/ADR cells after various treatments. **c** Mitochondrial membrane potential of MCF7/ADR cells after different treatments measured by JC-1 staining. **d** Cell mitochondrial stress and OCR determination of cells treated with various treatments. Abbreviations: Oligo, oligomycin, 30 μM, an ATP synthase inhibitor; FCCP, carbonyl cyanide 4-(trifluoromethoxy) phenylhydrazone, 2.5 μM, a mitochondrial uncoupler; AA/Rot: antimycin A/rotenone, 5 μM, complex III and I inhibitor. Western blot analysis of COX IV **e** and P-gp **f** after various treatments (Experiments were repeated three times). The uncropped scans of the blots are provided in Source Data files. **g** Confocal images of P-gp after various treatments in MCF7/ADR cells. Blue: Hoechst 33342, green: Alexa Fluor®488-conjugated P-gp secondary antibody. **h** Intensity of COX IV in MCF7/ADR cells. **i** Quantification of the DOX efflux rate after various treatments in MCF7/ADR cells. **j** CLSM image observation of DOX uptake in MCF7/ADR and MCF7 cells after different treatments. Blue: Hoechst 33342, red: DOX. **k** In vitro cytotoxicity after treatment with SNP$_{p\text{-}DOX}$ and inSNP$_{p\text{-}DOX}$ in MCF7, MCF7/ADR and HUVEC cells. **l** Schematic showing the procedures for analysis of DOX contents in tumor tissue MCF7/ADR tumor model. **m** HPLC profiles of DOX and p-DOX in tumor tissue after *i.v.* injection of free DOX, SNP$_{p\text{-}DOX}$ and inSNP$_{p\text{-}DOX}$. **n** Quantification of DOX content in tumor tissue at 12 h postinjection. Data denote mean ± s.d. ($n = 3$ independent samples). Statistical differences were analyzed by Student's *t*-test (two tails). $^{**}P < 0.01$, $^{***}P < 0.001$. Source data are provided as a Source Data file. Figures 5a and 5l, created with BioRender.com, were released under a Creative Commons Attribution-NonCommercial-NoDerivs 4.0 International license.

https://doi.org/10.1038/s41467-024-52006-0

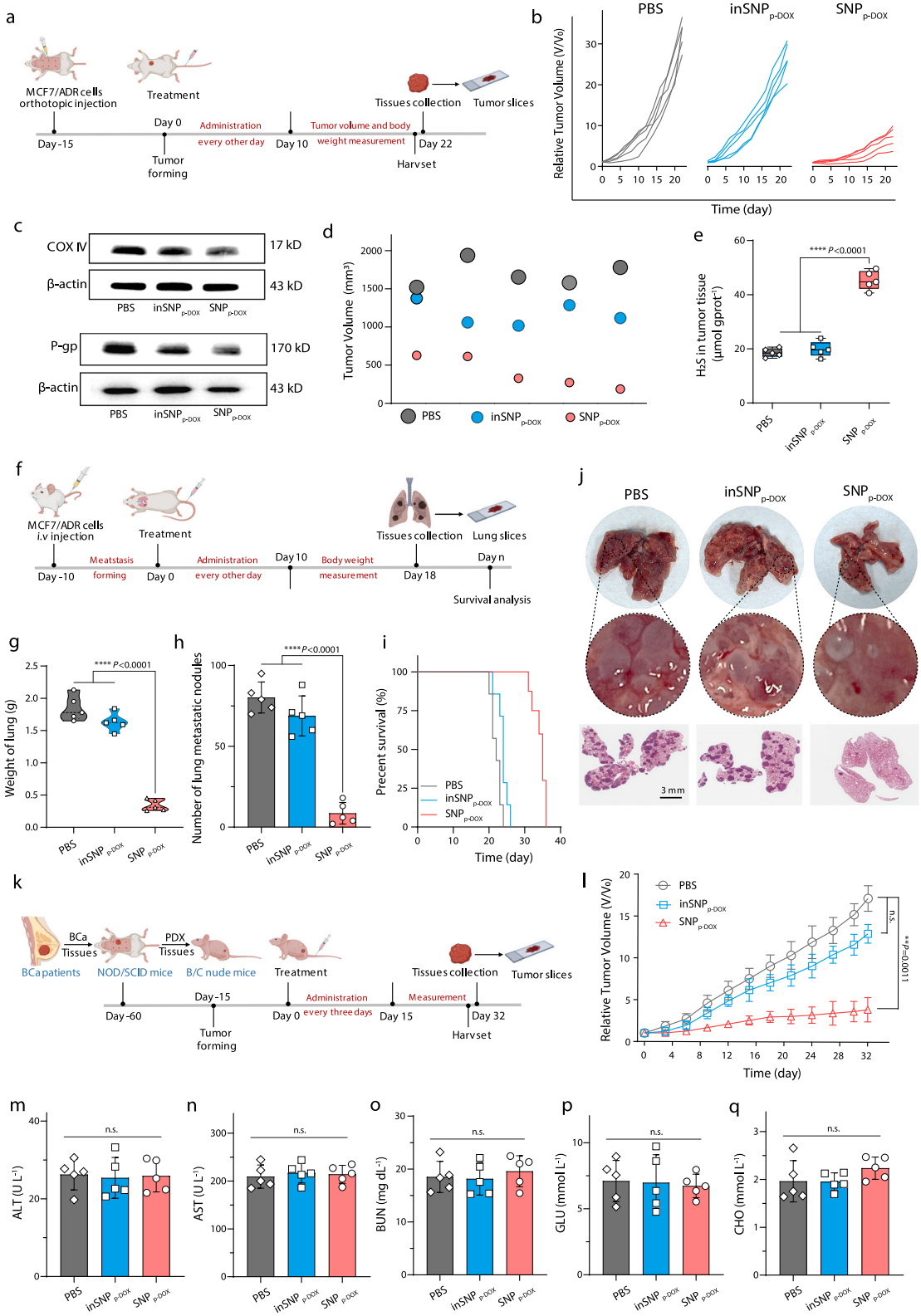

chemistry or caused any visible toxicity to the liver and kidney (Fig. 6m–q). In summary, these findings suggested that $SNP_{p\text{-}DOX}$ was biocompatible in vivo.

Discussion

Herein, we described a H_2S-responsive SNP that can amplify the H_2S signal at lesion sites for precisive cancer imaging and therapy. The kinetics of H_2S release showed that PTC could rapidly amplify the H_2S signal. Furthermore, we also demonstrated that the H_2S-triggered SNP disintegration process was a self-amplifying backbone degradation cascade and nanoparticle disassembly (Fig. 2).

A H_2S-responsive fluorescent probe based on hemicyanine dye (p-Cy) was used to fabricate nanoprobes ($SNP_{p\text{-}Cy}$) for the ultrasensitive detection of tumors. The high sensitivity, specificity activation, and

Fig. 6 | In vivo antitumor efficacy of $SNP_{p\text{-}DOX}$. **a** Schematic diagram of the tumor construction and treatment process for MCF7/ADR tumor-bearing NOD/SCID mice. **b** Individual tumor growth profiles of MCF7/ADR tumor-bearing mice from each treatment. **c** Change of COX IV and P-gp in tumors after treatment with various agents (Experiments were repeated three times). The uncropped scans of the blots are provided in Source Data files. **d** Tumor volume at day 22 after being treated with PBS, in$SNP_{p\text{-}DOX}$ and $SNP_{p\text{-}DOX}$. **e** The H_2S concentration in tumor tissue after treatment with various agents. The box plot shows the 25th percentile, the median, the 75th percentile, and minimum/maximum whiskers. **f** Metastatic tumor model treatment process via injection of MCF7/ADR cells into the tail vein. **g** Weight of lungs collected from mice at the end of the study. **h** Quantification of lung metastasis nodes per mouse from mice at the end of the study. **i** Survival rates of mice treated in different groups, $n = 7$ biologically independent animals. **j** Representative photographs H&E staining images of lung tissues collected at the end of the study. A representative image from one of five independent fields of view in a single experiment. **k** Treatment schedule for a PDX model. **l** Tumor growth inhibition study of PDX breast cancer. **m**–**q** The concentrations of ALT (**m**), AST (**n**), BUN (**o**), GLU (**p**) and CHO (**q**) in the serum after different treatments. Data denote mean ± s.d. ($n = 5$ independent samples). Statistical differences were analyzed by Student's *t*-test (two tails). $^{**}P < 0.01$, $^{****}P < 0.0001$, n.s., no significant difference. Source data are provided as a Source Data file. Figures 6a, 6f, and 6k, created with BioRender.com, were released under a Creative Commons Attribution-NonCommercial-NoDerivs 4.0 International license.

amplification H_2S signal of $SNP_{p\text{-}Cy}$ were confirmed in vitro and in vivo (Figs. 3, 4). The orthotopic liver tumor model demonstrated that $SNP_{p\text{-}Cy}$ can accurately delineate tumor margins for tumor resections. In addition, $SNP_{p\text{-}Cy}$ showed a good SBR to clearly define small cancer (<2 mm) via ultrasensitive imaging in metastatic lung cancer and orthotopic colorectal cancer models.

We then encapsulated H_2S-responsive anticancer prodrug of doxorubicin (p-DOX) in H_2S–PTC–PEG to manufacture a H_2S-responsive nanomedicine ($SNP_{p\text{-}DOX}$) with localized H_2S signal amplification for overcoming cancer drug resistance. In vitro studies confirmed that the $SNP_{p\text{-}DOX}$-induced endogenous H_2S elevation disrupted mitochondrial function and affected the function of the P-gp, leading to increased prodrug activation and MDR reversal (Fig. 5). In vivo studies confirmed that $SNP_{p\text{-}DOX}$ treatment significantly inhibited tumor growth in the MCF7/ADR xenograft tumor, breast cancer lung metastasis, and breast cancer PDX models (Fig. 6).

Thus, we successfully developed a self-immolation nanoplatform with localized H_2S signal amplification capabilities and demonstrated its utility for the ultrasensitive detection of small tumors and elevation of endogenous H_2S combined with prodrug activation to overcome drug resistance of cancer. We believe that this nanoplatform may provide a powerful tool for precise diagnosis and effective treatment of tumors.

Methods

Our research complies with all relevant ethical regulations of the South China University of Technology and the University of Science and Technology of China. All animal protocols were approved by the Animal Experiment Ethics Committee of the South China University of Technology (Approved number: AEC2018003) and were performed following the guidelines for the use of laboratory animals. The female mice with orthotopic tumors, authorized by the Committees on Animal Research and Ethics, consistently follow the humane endpoint. If the animal starts showing signs of immobility, a huddled posture, the inability to eat, ruffled fur, or self-mutilation, the animal will be euthanized immediately. The subcutaneous tumor maximum diameter was 20 mm and authorized by the Committees on Animal Research and Ethics and was not exceeded at any time during the experiments.

Chemicals and materials

Unless stated otherwise, all chemicals were bought from Energy Chemical (Shanghai, China) and utilized without additional purification. Doxorubicin hydrochloride (DOX·HCl) was purchased from Dalian Meilun Biotechnology Co., Ltd. (China). The mPEG-COOH was acquired from JenKen Co. LTD. (Beijing, China). Alexa Fluor®488 anti-mouse antibody was obtained from Abcam (Shanghai, China). Hoechst 33342 was received from Life Technologies. MTT and mitochondrial membrane potential fluorescent probe (JC-1 dye) were obtained from Sigma-Aldrich. The Hydrogen Sulfide (H_2S) Colorimetric Assay Kit was obtained from Elabscience Biotechnology.

Syntheses

Synthesis of H_2S–PTC. 4-isocyanatobenzyl alcohol (0.45 g, 2.7 mmol) and DBTDL (55 μL, 0.09 mmol) were dissolved in DMF (1 mL), preheated to 65 °C, and the reaction mixture was stirred in the glovebox under an inert atmosphere of N_2 for 7 h. (4-(2,4-dinitrophenoxy) phenyl) methanol (compound **2**, 0.52 g, 1.8 mmol), dissolved in anhydrous DMF (0.1 mL), was then added and the reaction was stirred for an additional 16 h. After cooling to room temperature, the polymer was precipitated from ether. The final product was obtained as a yellow solid (0.25 g, yield: 45%).

Synthesis of p-Cy. To a solution of 2,4-dinitrofluorobenzene (0.12 g, 0.65 mmol) and CyOH (0.25 g, 0.63 mmol) in DCM (8 mL), DIPEA (0.08 g, 0.63 mmol) was added dropwise, and the reaction mixture was stirred at 60 °C in the dark under an inert atmosphere of N_2 for 16 h. Subsequently, the crude product was purified by a silica gel column to afford p-Cy as a blue solid (0.17 g, yield: 48%).

Synthesis of p-DOX. DOX·HCl (0.21 g, 0.36 mmol) and TEA (0.15 mL, 1.1 mmol) were dissolved in DMF (20 mL), and stirred at room temperature under an inert atmosphere of N_2 for 12 h. Then, the reaction mixture was supplemented with 4-(2,4-dinitrophenoxy) benzyl (4-nitrophenyl) carbonate (0.20 g, 0.44 mmol, dissolved in 1 mL DMF) at room temperature for 24 h. After that, the solution was evaporated at reduced pressure and extracted with DCM to get the crude product. The crude product was purified by column chromatography on silica gel to afford p-DOX as a red solid (0.14 g, yield: 45%).

H_2S calibration curve

The methylene blue (MB) colorimetric method was used for H_2S detection. The MB cocktail solution was a mixture of 200 μL of 20 mM *N, N*-dimethyl-*p*-phenylenediamine dihydrochloride (DPD) in 7.2 M HCl, 200 μL of 30 mM $FeCl_3$ in 1.2 M HCl, and 100 μL of 1% (w/v) $Zn(OAc)_2$. In addition, a 1 mM stock solution of NaHS in 20 mM PBS was fabricated in the N_2-filled glovebox. 500 μL of MB cocktail solution was added into 2 mL microcentrifuge tubes, and subsequently, a NaHS stock solution was added to achieve the desired final H_2S concentrations of 1, 3, 5, 10, 20, 40, 60, 80, 100, and 200 μM. The MB solution was reacted with H_2S for 30 minutes and then measured the absorbance at 670 nm.

Preparation of nanoparticles

Dissolve H_2S–PTC–PEG or Ctrl–PTC–PEG (10 mg) and p-Cy or p-DOX (1 mg) in 1 mL DMSO, followed by dropping into 9 mL water and stirring at room temperature for 4 h. The mixtures were placed into the dialysis membrane tubing (MWCO = 3500 Da) and subjected to dialysis against water for 24 h. The p-Cy or p-DOX concentration were determined by multi-functional microporous plate analysis system (Biotek Cytation5, United States) at 590 nm or 480 nm by UV absorption.

Measurement of the detection limit

The detection limit (LOD) of $SNP_{p\text{-}Cy}$ or control small molecule p-Cy for H_2S was determined as follows: LOD = 3σ/k. The standard deviation was represented by σ, while the slope of titration spectra curve within

the limited range was represented by k.Briefly, the fluorescence emission spectrum of $SNP_{p\text{-}Cy}$ or p-Cy (10 μM) in 20 mM PBS buffer contained 2% (v/v) DMSO and 25 μg mL^{-1} CA, was measured for 10 times to determine the background noise σ. Then the solution was added with different concentrations of H_2S (0–200 μM), and all spectra were recorded 30 min post each addition. A linear regression curve was then fitted according to the fluorescence intensity changes at lower concentrations, and the slope of the curve (*k*) was obtained.

Cells and animals

4T1 and MCF7 breast carcinoma, CT26 and HCT116 colorectal carcinoma, Hepa 1-6 and HepG2 hepatocellular carcinoma, Hela adenocarcinoma, B16F10 melanoma, GL261 brain glioma cells, L929 fibroblast and HUVEC epithelial were obtained from the American Type Culture Collection (ATCC). All cell lines were cultured in complete medium (RPMI 1640 or DMEM with 10% FBS and 1% antibiotics) in a humidified atmosphere containing 5% CO_2 at 37 °C. DOX·HCl (1 μg mL^{-1}) was added into MCF7/ADR culture medium to maintain drug resistance phenotype.

Female BALB/c nude mice, female BALB/c mice, female NOD/SCID mice, and female ICR mice were acquired from Hunan SJA Laboratory Animal Co., Ltd (Hunan, China). Animals were housed in a controlled environment, maintained a temperature of around 25°C and humidity 50 ± 10% with a 12 h light/dark cycle. Maximal tumor burden permitted is 2,000 mm^3, and the maximum tumor size did not surpass in all experiments. The South China University of Technology Animal Care and Use Committee approved all procedures (Approved number: AEC2018003), and the care and use of mice in accordance with the Guide for the Care and Use of Laboratory Animals. The PDX tumor tissues used in this study were obtained from the First Affiliated Hospital of Sun Yat-sen University and Nanfang Hospital and ethically approved by the two hospitals. All patients gave written informed consent in the study.

Fluorescence recovery imaging of cells

CT26, Hepa 1-6 and L929 cells (2×10^5 cells per well) were cultured on glass coverslips overnight, then exposed to CyOH, p-Cy, $SNP_{p\text{-}Cy}$, and $inSNP_{p\text{-}Cy}$ at the same dose (1 μg mL^{-1}) for 4 h. The nuclei were marked with Hoechst 33342 for 15 min and then imaged by CLSM.

CT26 cells were cultured in 6 well plates (1×10^6 cells per well). Cells were treated with $SNP_{p\text{-}Cy}$ (4 μg mL^{-1}) together with 300 μM $ZnCl_2$ (incubation in advance for 10 min), 1 mM NaHS (incubation in advance for 1 h), 200 μM L-Cys (incubation in advance for 1 h). The cell pellets were then collected and immediately imaged on the IVIS Spectrum imaging system. The Living Image Software was utilized to measure the fluorescence intensities in the cell pellets.

CT26, Hepa 1-6 and L929 cells (1×10^4 cells per well) were cultured in 96 well black culture plates. Upon co-incubation p-Cy (4 μg mL^{-1}) with varying concentrations of SNP or inSNP at the desired concentrations for 12 h, cells were washed three times with PBS, and then directly imaged by an IVIS Spectrum imaging system.

Oxygen consumption rate (OCR) detection

OCR was measured with an XF96 extracellular flux analyzer (Seahorse Bioscience) in accordance with the manufacturer's recommended protocols. Briefly, MCF7/ADR cells were seeded on XF96 microplates (1×10^4 cells per well) that had been pre-coated with Cell-Tak adhesive (BD Biosciences). The plates were rapidly centrifuged to immobilize cells. Then cells were cultured in a non-buffered assay medium (Seahorse Biosciences) and incubated in a non-CO_2 environment overnight before assay. Cells were treated with PBS, $SNP_{p\text{-}DOX}$ and $inSNP_{p\text{-}DOX}$ (DOX: 4 μg mL^{-1}) for 6 h and abandoned the medium. Three baseline records were taken, and then serial injection of 30 μM oligomycin, 2.5 μM FCCP, and 5 μM antimycin A /rotenone.

Study on the distribution and changes of P-gp

MCF7/ADR cells (1×10^5 cells per well) were cultured on 24 well plates and exposed to PBS, $SNP_{p\text{-}DOX}$, and $inSNP_{p\text{-}DOX}$ (DOX: 4 μg mL^{-1}) for 12 h, fixed with 4% formaldehyde, then blocked with 5% BSA-PBS for 4 h at room temperature. Cells were incubated with a P-gp monoclonal antibody in 0.1% BSA-PBS at a dilution of 1:20 overnight at 4 °C. Then cells were washed with PBS and incubated with Alexa Fluor®488-conjugated secondary antibody in 0.1% BSA-PBS at a dilution of 1:500 for 3 h at room temperature in the dark. The nuclei were marked with Hoechst 33342 for 15 min and then imaged by CLSM.

Cytotoxicity assay

MCF7, MCF7/ADR, or HUVEC cells were seeded in 96-well culture plates (1×10^4 cells per well) and incubated for 12 h. The cells were then treated with DOX, p-DOX, SNP, inSNP, $SNP_{p\text{-}DOX}$, and $inSNP_{p\text{-}DOX}$ at the desired concentrations. The cell viability was measured by MTT assay after 24 h of cell culture.

MCF7/ADR cells (5×10^5 cells per well) were seeded in 6-well plates overnight. The cells were treated with PBS, DOX, p-DOX, $SNP_{p\text{-}DOX}$, and $inSNP_{p\text{-}DOX}$ for 12 h. After exposure, collected cells and stained by using the Annexin V-FITC/7-AAD Apoptosis Detection Kit. Cells were rinsed three times with PBS, collected, and analyzed by Flow Cytometry.

In Vivo and ex vivo fluorescence imaging

All the tumor-bearing female mice were intravenously injected with $SNP_{p\text{-}Cy}$ or $inSNP_{p\text{-}Cy}$ (1 mg kg^{-1}) for fluorescence imaging by an IVIS Spectrum imaging system (E_x/E_m = 660/750 nm). Whereafter, mice were killed and harvested tumors and major organs for ex vivo imaging.

Activation of p-DOX in tumor and major organs

Female BALB/c nude mice bearing MCF7/ADR tumors were sacrificed by cervical vertebra dislocation at 12 h post-injection of DOX, p-DOX, $SNP_{p\text{-}DOX}$ and $inSNP_{p\text{-}DOX}$ (DOX: 5 mg kg^{-1}), the tumors and major organs were collected. The prodrug activation of p-DOX in vivo was analyzed by HPLC (Waters e2965) equipped with a XBridge® C18 column (5 μm 4.6 × 100 mm), using 3/1 (v/v) acetonitrile/water containing 5% (v/v) acetic acid as the mobile phase (1.0 mL min^{-1}). The eluent was excited with a 495 nm laser and monitored at 595 nm.

Tumor growth inhibition in vivo

All the tumor-bearing female mice were randomized into three groups (n = 5), intravenously administrated PBS, $SNP_{p\text{-}DOX}$ and $inSNP_{p\text{-}DOX}$ at an equivalent DOX dose (DOX: 5 mg kg^{-1}), respectively, and the tumor volume and body weight were measured and recorded in each mouse during treatment.

Statistical analysis

All data were presented as mean ± standard deviation. Analyzing the statistical differences between experimental groups with Student's *t*-test (two tails). $P < 0.05$ was considered statistically significant. All statistical calculations were performed by GraphPad Prism software (PRISM 8.0, GraphPad Prism Software).

Reporting summary

Further information on research design is available in the Nature Portfolio Reporting Summary linked to this article.

Data availability

The data generated in this study are available within the Article, Supplementary Information, Source Data file, and from corresponding author(s) upon request. Source data are provided with this paper.

References

1. Szabo, C. Hydrogen sulphide and its therapeutic potential. *Nat. Rev. Drug Discov.* **6**, 917–935 (2007).
2. Paul, B. D. & Snyder, S. H. H_2S signalling through protein sulfhydration and beyond. *Nat. Rev. Mol. Cell Biol.* **13**, 499–507 (2012).
3. Wallace, J. L. & Wang, R. Hydrogen sulfide-based therapeutics: exploiting a unique but ubiquitous gasotransmitter. *Nat. Rev. Drug Discov.* **14**, 329–345 (2015).
4. Hartle, M. D. & Pluth, M. D. A practical guide to working with H_2S at the interface of chemistry and biology. *Chem. Soc. Rev.* **45**, 6108–6117 (2016).
5. Fiorucci, S. et al. The third gas: H_2S regulates perfusion pressure in both the isolated and perfused normal rat liver and in cirrhosis. *Hepatology* **42**, 539–548 (2005).
6. Ning, N. et al. Dysregulation of hydrogen sulphide metabolism impairs oviductal transport of embryos. *Nat. Commun.* **5**, 4107 (2014).
7. Szabo, C. Gasotransmitters in cancer: from pathophysiology to experimental therapy. *Nat. Rev. Drug Discov.* **15**, 185–203 (2016).
8. Wang, Y., Yang, T. & He, Q. Strategies for engineering advanced nanomedicines for gas therapy of cancer. *Natl Sci. Rev.* **7**, 1485–1512 (2020).
9. Wu, L. et al. H_2S-activatable near-infrared afterglow luminescent probes for sensitive molecular imaging in vivo. *Nat. Commun.* **11**, 446 (2020).
10. Liu, B. et al. A tumor-microenvironment-responsive nanocomposite for hydrogen sulfide gas and trimodal-enhanced enzyme dynamic therapy. *Adv. Mater.* **33**, 2101223 (2021).
11. Yang, Z. et al. Photothermo-promoted nanocatalysis combined with H_2S-mediated respiration inhibition for efficient cancer therapy. *Adv. Funct. Mater.* **31**, 2007991 (2021).
12. Li, J. et al. A metal-phenolic nanosensitizer performs hydrogen sulfide-reprogrammed oxygen metabolism for cancer radiotherapy intensification and immunogenicity. *Angew. Chem. Int. Ed.* **61**, 202200830 (2022).
13. Levinn, C. M., Cerda, M. M. & Pluth, M. D. Development and application of carbonyl sulfide-based donors for H_2S delivery. *Acc. Chem. Res.* **52**, 2723–2731 (2019).
14. Urquhart, M. C. et al. Recent advances in the delivery of hydrogen sulfide via a macromolecular approach. *Polym. Chem.* **9**, 4431–4439 (2018).
15. Powell, C. R., Dillon, K. M. & Matson, J. B. A review of hydrogen sulfide (H_2S) donors: Chemistry and potential therapeutic applications. *Biochem. Pharmacol.* **149**, 110–123 (2018).
16. Hu, J. et al. Engineering macromolecular nanocarriers for local delivery of gaseous signaling molecules. *Adv. Drug Deliv. Rev.* **179**, 114005 (2021).
17. Zhao, Y. & Pluth, M. D. Hydrogen sulfide donors activated by reactive oxygen species. *Angew. Chem. Int. Ed.* **128**, 14638–14642 (2016).
18. Rong, F. et al. Intelligent polymeric hydrogen sulfide delivery systems for therapeutic applications. *Bioact. Mater.* **19**, 198–216 (2023).
19. Stuart, M. A. et al. Emerging applications of stimuli-responsive polymer materials. *Nat. Mater.* **9**, 101–113 (2010).
20. Mo, R. & Gu, Z. Tumor microenvironment and intracellular signal-activated nanomaterials for anticancer drug delivery. *Mater. Today* **19**, 274–283 (2016).
21. Kamaly, N., Yameen, B., Wu, J. & Farokhzad, O. C. Degradable controlled-release polymers and polymeric nanoparticles: mechanisms of controlling drug release. *Chem. Rev.* **116**, 2602–2663 (2016).
22. Dong, Y. et al. A general strategy for macrotheranostic prodrug activation: synergy between the acidic tumor microenvironment and bioorthogonal chemistry. *Angew. Chem. Int. Ed.* **59**, 7168–7172 (2020).
23. Yang, G., Liu, Y., Chen, J., Ding, J. & Chen, X. Self-adaptive nanomaterials for rational drug delivery in cancer therapy. *Acc. Chem. Res.* **3**, 1232–1247 (2022).
24. Mitchell, M. J. et al. Engineering precision nanoparticles for drug delivery. *Nat. Rev. Drug Discov.* **20**, 101–124 (2021).
25. Dong, Y. et al. Mitochondria-targeting Cu_3VS_4 nanostructure with high copper ionic mobility for photothermoelectric therapy. *Sci. Adv.* **9**, eadi9980 (2023).
26. Blum, A. P. et al. Stimuli-responsive nanomaterials for biomedical applications. *J. Am. Chem. Soc.* **137**, 2140–2154 (2015).
27. Seidi, F., Jenjob, R. & Crespy, D. Designing smart polymer conjugates for controlled release of payloads. *Chem. Rev.* **118**, 3965–4036 (2018).
28. Sagi, A., Weinstain, R., Karton, N. & Shabat, D. Self-immolative polymers. *J. Am. Chem. Soc.* **130**, 5434–5435 (2008).
29. Liu, G., Wang, X., Hu, J., Zhang, G. & Liu, S. Self-immolative polymersomes for high-efficiency triggered release and programmed enzymatic reactions. *J. Am. Chem. Soc.* **136**, 7492–7497 (2014).
30. Shelef, O., Gnaim, S. & Shabat, D. Self-Immolative polymers: an emerging class of degradable materials with distinct disassembly profiles. *J. Am. Chem. Soc.* **143**, 21177–21188 (2021).
31. Wang, K. et al. Self-immolative polyprodrug-based tumor-specific cascade amplificated drug release nanosystem for orchestrated synergistic cancer therapy. *Biomaterials* **289**, 121803 (2022).
32. Buddingh', B. C., Elzinga, J. & van Hest, J. Intercellular communication between artificial cells by allosteric amplification of a molecular signal. *Nat. Commun.* **11**, 1652 (2020).
33. Wong, A. D., DeWit, M. A. & Gillies, E. R. Amplified release through the stimulus triggered degradation of self-immolative oligomers, dendrimers, and linear polymers. *Adv. Drug Deliv. Rev.* **64**, 1031–1045 (2012).
34. Yoshii, T., Onogi, S., Shigemitsu, H. & Hamachi, I. Chemically reactive supramolecular hydrogel coupled with a signal amplification system for enhanced analyte sensitivity. *J. Am. Chem. Soc.* **137**, 3360–3365 (2015).
35. Mi, P. et al. A pH-activatable nanoparticle with signal-amplification capabilities for non-invasive imaging of tumour malignancy. *Nat. Nanotechnol.* **11**, 724–730 (2016).
36. Zheng, X. et al. Successively activatable ultrasensitive probe for imaging tumour acidity and hypoxia. *Nat. Biomed. Eng.* **1**, 57 (2017).
37. Zhu, Y. et al. Dual nanozyme-driven PtSn bimetallic nanoclusters for metal-enhanced tumor photothermal and catalytic therapy. *Acs Nano.* **17**, 6833–6848 (2023).
38. Dong, S. et al. Electron transport chain interference" strategy of amplified mild-photothermal therapy and defect-engineered multienzymatic activities for synergistic tumor-personalized suppression. *J. Am. Chem. Soc.* **145**, 9488–9507 (2023).
39. Zhao, R. et al. Architecture of Vanadium-based MXene dysregulating tumor redox homeostasis for amplified nanozyme catalytic/photothermal therapy. *Adv. Mater.* **36**, 2307115 (2024).
40. Zhu, Y. et al. Defect-engineered tin disulfide nanocarriers as "Precision-Guided Projectile" for intensive synergistic therapy. *Small Methods*, 2400125 https://doi.org/10.1002/smtd.202400125 (2024).
41. Miller, K. A. et al. Acid-triggered, acid-generating, and self-amplifying degradable polymers. *J. Am. Chem. Soc.* **141**, 2838–2842 (2019).
42. Tan, J. et al. Coordinating external and built-in triggers for tunable degradation of polymeric nanoparticles via cycle amplification. *J. Am. Chem. Soc.* **143**, 13738–13748 (2021).
43. Xu, J. et al. Self-immolative amphiphilic poly(ferrocenes) for synergistic amplification of oxidative stress in tumor therapy. *Angew. Chem. Int. Ed.* **62**, 202303829 (2023).
44. Powell, C. R. et al. Self-amplified depolymerization of Oligo(thiourethanes) for the release of COS/H_2S. *Polym. Chem.* **10**, 2991–2995 (2019).
45. Szabo, C. et al. Tumor-derived hydrogen sulfide, produced by cystathionine-beta-synthase, stimulates bioenergetics, cell proliferation, and angiogenesis in colon cancer. *Proc. Natl Acad. Sci. USA* **110**, 12474–12479 (2013).

46. Hammers, M. D. et al. A bright fluorescent probe for H_2S enables analyte-responsive, 3D imaging in live Zebrafish using light sheet fluorescence microscopy. *J. Am. Chem. Soc.* **137**, 10216–10223 (2015).
47. Fu, M. et al. Hydrogen sulfide (H_2S) metabolism in mitochondria and its regulatory role in energy production. *Proc. Natl Acad. Sci. USA* **109**, 2943–2948 (2012).
48. Huang, D., Jing, G. & Zhu, S. Regulation of mitochondrial respiration by hydrogen sulfide. *Antioxidants* **12**, 1644 (2023).

Acknowledgements

This work was supported by the National Key R&D Program of China (No.2022YFB3804700 Y.Y.), the National Natural Science Foundation of China (No.52073101 Y.Y.), Guangdong Provincial Pearl River Talents Program (No.2019QN01Y088 Y.Y.) and Guangdong Basic and Applied Basic Research Foundation (No.2021A1515110258, 2023A1515011493 K.W.).

Author contributions

Q.Z. and J.L. performed the experiments. Q.X. and Y.L. helped with the in vitro and in vivo experiments. Q.Z. and J.L. contributed to the scheme and figures. K.W. and Y.Y. discussed the data. Q.Z. prepared the original draft. Y.Y. contributed to the revision of the original draft. Q.Z., J.L. and Y.Y. conceived the idea and designed the experimental plan. All the authors discussed the results and commented on the manuscript.

Competing interests

The authors declare no competing interests.

Additional information

Supplementary information The online version contains supplementary material available at https://doi.org/10.1038/s41467-024-52006-0.

Correspondence and requests for materials should be addressed to Youyong Yuan.

Peer review information *Nature Communications* thanks Haibin Shi and the other, anonymous, reviewer(s) for their contribution to the peer review of this work. A peer review file is available.